General-relativistic treatment of tidal *g*-mode resonances in coalescing binaries of neutron stars – I. Theoretical framework and crust breaking

Hao-Jui Kuan [1,2]★ Arthur G. Suvorov[1] and Kostas D. Kokkotas[1]

[1]*Theoretical Astrophysics, Eberhard Karls University of Tübingen, Tübingen, D-72076, Germany*
[2]*Department of Physics, National Tsing Hua University, Hsinchu 300, Taiwan*

ABSTRACT

During the final stages of a neutron-star binary coalescence, stellar quasi-normal modes can become resonantly excited by tidal fields. If the strain exerted by the excited modes exceeds the extent to which the crust can respond linearly, localized crustal failures may occur. In this work, we re-examine resonant *g*-mode excitations of relativistic neutron stars in the last ~ 10 s of an inspiral. We adopt realistic equations of state that pass constraints from GW170817, include third-order post-Newtonian terms for the conservation orbital motion, and employ a 2.5 post-Newtonian scheme for gravitational back-reaction. Frequency modulations of the modes due to tidal fields, Lorentz forces, and (slow) rotation are also considered to investigate the maximal strain achievable by resonantly excited *g* modes. Depending on the equation of state, degree of stratification, and stellar magnetic field, we find that certain *g*-mode excitations may be able to break the crust some seconds prior to coalescence.

Key words: methods: numerical – binaries: close – stars: magnetic field – stars: neutron – stars: oscillations – stars: rotation.

1 INTRODUCTION

Tidal effects in compact binary systems containing at least one neutron star (NS) may be studied by both electromagnetic and gravitational-wave (GW) measurements (Abbott et al. 2017a,b,c). Such studies allow one to probe the fundamental properties of the progenitor NSs, such as the equation of state (EOS; Abbott et al. 2018; Radice et al. 2018). In the final stages of a merger, orbital energy and stellar internal energy are redistributed efficiently by tidal force(s) and dissipation. The former excites stellar quasi-normal modes (QNMs), leading to the transfer of orbital energy into excited modes, thus leaving certain imprints into the orbit evolution (e.g. accelerating coalescence and causing shifts in the GW phase by *f*-mode excitations Kokkotas & Schafer 1995; Vick & Lai 2019). The latter, resulting from viscosity, damps the excited modes, turning kinetic energy into thermal energy, which can heat up the star to $\sim 10^8$ K before merger (Lai 1994). In particular, when the tidal-perturbing frequency matches the eigenfrequency of a particular QNM at some point prior to merging, the mode becomes resonantly excited. Mode amplitudes increase rapidly during a period of resonance, possibly straining the crust to the point that quake or fracture events can occur (Horowitz & Kadau 2009; Baiko & Chugunov 2018). It has been suggested that localised failure events offer a possible mechanism (Tsang et al. 2012; Suvorov & Kokkotas 2020; Passamonti, Andersson & Pnigouras 2021) to trigger 'precursor' events of short gamma-ray bursts (Troja, Rosswog & Gehrels 2010).

In general, identifying the precise conditions under which crustal failure can occur is complicated. In addition to the actual physics of fracturing not being perfectly understood (see section 2.2 of Lander & Gourgouliatos 2019, for a discussion), many factors participate in the straining mechanism, such as: the mass ratio of the binary (Hinderer et al. 2016; Steinhoff et al. 2016), the structure and strength of the stellar magnetic field (Nasiri & Sobouti 1989; Suvorov & Kokkotas 2020), the degree of stellar stratification, which affects the *g*-mode spectrum in particular (Xu & Lai 2017; Passamonti et al. 2021), the rotation rate (Yoshida & Eriguchi 1999; Gaertig & Kokkotas 2009; Krüger & Kokkotas 2020), and the stellar EOS that characterizes the internal structure (Lattimer & Prakash 2001; Zhou & Zhang 2017). Electromagnetic byproducts of crustal failures, such as precursor events, may therefore deliver useful information about stellar behaviour in the final stages of coalescing binaries.

Moreover, NSs are compact enough that relativistic effects are not negligible in these last stage. For instance, QNM eigenfrequencies can differ from their Newtonian counterparts by $\gtrsim 10$ per cent (Chan et al. 2014), which, if unaccounted for, results in errors in the estimation of parameters that allow for resonances to happen at certain times. Building on previous studies (Tsang et al. 2012; Suvorov & Kokkotas 2020; Passamonti et al. 2021), we introduce a general-relativistic framework in this study that aims to (at least phenomenonologically) incorporate each of the above elements to better understand the connection between resonantly excited modes and crust yielding. This is the first of two papers in a series, where the framework is detailed. In a forthcoming paper (paper II), the aforementioned electromagnetic byproducts are examined in detail and compared with the results obtained herein.

★ E-mail: hao-jui.kuan@uni-tuebingen.de

At the non-rotating level,[1] the QNMs of NSs can be generally resolved into *p*, *f*, *w*, and *g* modes. Since the (rotating-frame) frequencies of the stellar *g* modes, which are QNMs restored by buoyancy, are typically in the hundreds of Hz (McDermott, van Horn & Scholl 1983; Finn 1987; McDermott 1990; Xu & Lai 2017), these modes are generally thought to lie in the sweet spot of the precursor scenario (that is, they match well with the expected driving frequency at the time when precursors are observed relative to the main burst; cf. paper II). We derive empirical relations for EOS- and stratification-related effects on the *g*-mode eigenfrequencies. Shifts in the spectra due to magnetic fields (Section 5.1), tidal fields (Section 5.2), and rotation (Section 5.3) are also considered. In principle, interface modes (McDermott et al. 1985; McDermott, van Horn & Hansen 1988; Piro & Bildsten 2005) and shear modes (Schumaker & Thorne 1983; Sotani, Kokkotas & Stergioulas 2007; Vavoulidis, Kokkotas & Stavridis 2008; Sotani 2016) could potentially be responsible for precursors as well (Passamonti et al. 2021). However, the stars considered here have neither phase transitions that result in density jumps inside the star, nor a solid crust separated from the fluid core, hence those modes are absent.

This paper is organized as follows. We write down the equations of stellar structure relevant for the EOS considered here (Section 2.1). Numerical details concerning the calculation of QNMs, with a specific focus on the *g* modes, is also given (Section 2.2). The orbital dynamics and relevant assumptions concerning the binary itself are given in Section 3. Magnetic fields with hybrid structure on a relativistic star is derived in Section 4. In Section 5 we study mode modulations by tidal, magnetic, and centrifugal forces and the strain generated by excited modes is investigated in Section 6. A discussion is offered in Section 7.

Except where stated otherwise, quantities are expressed in natural units with $c = G = 1$, Greek letters denote four-dimensional space–time indices with an exception of α, which denotes the quantum number of eigenmodes, and Latin indices refer to the spatial three components. We adopt the following notation for compactness throughout: $B_{15} = B_\star/(10^{15}\text{G})$, $M_{1.4} = M/(1.4\,\text{M}_\odot)$, and $R_{10} = R/(10\,\text{km})$, where $B_\star$ is the characteristic magnetic field strength that will be introduced in Section 4.1.

2 STELLAR STRUCTURE

We consider a static, spherically symmetric line element ,

$$ds^2 = -e^{2\Phi(r)}dt^2 + e^{2\lambda(r)}dr^2 + r^2(d\theta^2 + \sin^2\theta^2 d\phi^2), \quad (1)$$

where (t, r, θ, ϕ) are the usual Schwarzschild coordinates, and Φ and λ are functions of r only. The Einstein equations

$$G_{\mu\nu} = 8\pi T_{\mu\nu}, \quad (2)$$

for the stress-energy tensor associated with a single, perfect fluid,

$$T^{\mu\nu} = (\rho + p)u^\mu u^\nu + pg^{\mu\nu}, \quad (3)$$

describe the structure of a static, non-rotating star. Here ρ is the energy-density, p is the stellar pressure, $g_{\mu\nu}$ is the metric tensor defined in (1), and $u^\mu = e^{-\Phi}\delta_0^\mu \partial_t$ is the four-velocity of a generic

fluid element (rotational corrections to the stellar structure are considered in Section 5.3). The metric function λ is related to the mass distribution function $m(r)$, which yields the mass inside the circumferential radius r, through

$$e^{-2\lambda} = 1 - \frac{2m(r)}{r}. \quad (4)$$

The conservation law,

$$0 = \nabla^\mu T_{\mu\nu}, \quad (5)$$

relates the functions $\rho(r)$, and $p(r)$ to the metric variables, and forms the following system

$$\frac{d\Phi}{dr} = \frac{1}{p(r) + \rho(r)}\frac{dp}{dr}, \quad (6a)$$

$$\frac{dm}{dr} = 4\pi r^2 \rho(r), \quad (6b)$$

and

$$\frac{dp}{dr} = -\frac{[\rho(r) + p(r)]\left[m(r) + 4\pi r^3 p(r)\right]}{r^2\left[1 - \frac{2m(r)}{r}\right]}. \quad (6c)$$

The star's radius $R_\star$ and mass $M_\star$ are defined by the boundary conditions $p(R_\star) = 0$ and $m(R_\star) = M_\star$, respectively. Outside of the star, where $p = \rho = 0$, the metric (1) reduces to the Schwarzschild metric of mass $M_\star$.

2.1 Equation of state

We consider piecewise-polytropic approximations (Read et al. 2009) to three different realistic EOS, namely the APR4, SLy, and WFF families. We choose these models because they are sufficiently soft to be compatible with the tidal deformability measured in GW170817 (Abbott et al. 2018). The aforementioned EOS are all barotropic [i.e. $p = p(\rho)$], which is a reasonable approximation for mature systems older than the relevant electroweak and diffusion time-scales (Mastrano, Suvorov & Melatos 2015) where thermal fluxes are likely to be negligible, and the buoyancy comes primarily from composition gradients inside the star. Note, however, that tidal heating is expected to be able to raise the temperature of the (still relatively cold) NS crust to $\sim 10^8$ K prior to merger (Lai 1994). Thermal gradients may therefore become important at late times (Bauswein, Janka & Oechslin 2010).

While each EOS considered here assumes that the stars consist of $npe\mu$ nuclear matter, the many-body problem is handled differently:

(i) WFF families are obtained using variational methods applied to nucleon Hamiltonians, that contain pieces of two-body and three-body interactions. More precisely, different two- and three-nucleon potentials are used to model the bulk matter (see Wiringa, Fiks & Fabrocini 1988 for details).

(ii) SLy is derived from the Skyrme effective nucleon–nucleon interaction (Douchin & Haensel 2001), consistent with WFF2 in the regime where the baryon density exceeds the nuclear value $n_0 = 0.16$ fm^{-3}.

(iii) APR4 is derived by variational chain summation methods (Akmal, Pandharipande & Ravenhall 1998) adopting a two-nucleon interaction (Wiringa, Stoks & Schiavilla 1995) that accounts for Lorentz boost corrections not used in WFF1.

Masses $M_\star$ of the stars constructed with these EOS, as functions of central density, are shown in the upper panel of Fig. 1. The intersections of each curves with the dashed lines (both green and

---

[1]Because mature NSs as part of binary systems are expected to be slowly rotating (Bildsten & Cutler 1992; Kochanek 1992), the inertial- and rotating-frame frequencies of the modes roughly coincide. For rapidly rotating stars however, *r*- and even *f*-mode frequencies can be comparable with the frequency of tidal driving ∼seconds before merger (Pnigouras 2019; Suvorov & Kokkotas 2020); see Section 5.3 for a discussion on rotational corrections.
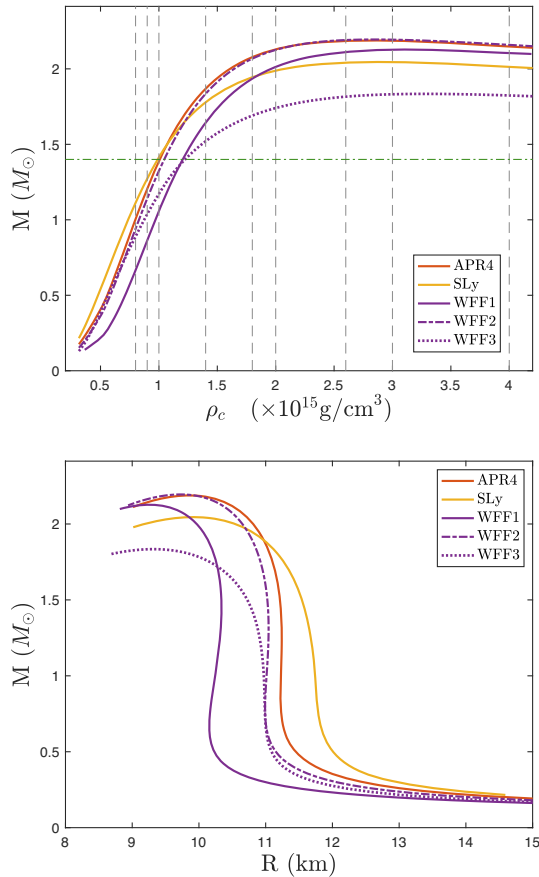
Figure 1. Mass of non-rotating equilibrium models constructed with various EOSs surviving the constraints of GW170817 (APR4, SLy, WFF1-3) as functions of central density (top panel) and stellar radius (bottom panel). We choose several models for each EOS to be studied. These models include those represented by the intersection of each EOS curve with the grey dashed lines, and those having masses of $1.4 \, M_\odot$ (the intersection of each EOS curve with the green dashed line).

grey) mark the models that we choose for later analysis. The mass–density relations [bottom panel of Fig. 1] tells us that the SLy EOS is the stiffest one and the WFF1 is the softest one.

2.2 g modes

Oscillatory patterns of motion in a star can be resolved into QNMs with complex eigenfrequency ω_α, where α denotes the ensemble of quantum numbers $\alpha = (nlm)$ for overtone number n, and spherical harmonic indices l and m. The oscillating frequency is the real part of ω_α, while the reciprocal of the imaginary part defines the damping rate due to radiation-reaction. In general, QNMs are categorized according to the nature of the restoring force. For example, p modes are supported by pressure, while g modes are supported by buoyancy. We focus on g modes in this work because they are more likely to become resonant in the last $\sim$10 s of inspirals for slowly-rotating NSNS mergers (though see footnote 1) since their (fundamental) frequencies are typically smaller than a few hundred Hz (Lai 1994; Kokkotas & Schafer 1995; Kantor & Gusakov 2014; Andersson & Ho 2018).

Inhomogeneities in composition and/or temperature give rise to stellar stratification and buoyancy as gravity tends to smooth out these gradients (McDermott et al. 1983; Finn 1987; Strohmayer 1991;

Reisenegger & Goldreich 1992). Explicitly, stratification prevents the Schwarzschild discriminant,

$$A := e^{-\lambda} \frac{dp}{dr} \frac{1}{p} \left(\frac{1}{\gamma} - \frac{1}{\Gamma} \right),\qquad(7)$$

from vanishing, where

$$\gamma = \frac{\rho + p}{p} \frac{dp}{d\rho},\qquad(8)$$

is the adiabatic index associated with the equilibrium star described in Section 2. The parameter Γ represents the adiabatic index of the *perturbation*, which need not match that of the background for non-isentropic perturbations (Lockitch, Andersson & Friedman 2001). Aiming to provide a proof-of-principle framework in this work, we introduce a phenomenological parameter δ that encapsulates the departure from isentropicity through

$$\Gamma = \gamma(1 + \delta).\qquad(9)$$

In principle, one could determine δ from first principles by calculating the sound speed and the determinant of the Brunt-Väisälä frequency from the nuclear Hamiltonian together with the Gibbs equation describing the evolution of the chemical composition (Reisenegger & Goldreich 1992; Lai 1994). However, here we approximate the EOS as barotropic, i.e. $p = p(\rho)$, which erases the compositional information in practice. The composition gradient, which offers buoyancy for g modes, is therefore, strictly speaking, absent. The artificial parameter Γ is used as a proxy for perturbation-induced changes in the chemical potentials resulting from a *non-adiabatic* perturbation. In addition, as shown by Reisenegger (2001), NSs are in general stably stratified due to the interior equilibrium composition gradient, implying $A < 0$ inside the star (i.e. $\gamma < \Gamma$). We thus consider positive δ hereafter.

The numerical calculation of the complex g-mode frequencies is known to be difficult because $|\text{Im}(\omega_\alpha)| \ll |\text{Re}(\omega_\alpha)|$, meaning that high precision is necessary to prevent errors in the real parts contaminating the imaginary parts, as discussed by Finn (1986). Searching for low-frequency g modes and their respective eigen-functions entails a delicate separation of the ingoing- and outgoing-waves at spatial infinity, so that one can impose the purely outgoing boundary condition.[2] Techniques based on *phase integrals* have been proven to be adequate for this purpose (Andersson, Kokkotas & Schutz 1995). On top of that, the minute displacements of g modes, which is translated from eigenfunctions, make the differential system of the eigenproblem put forward by Lindblom & Detweiler (1983) and Detweiler & Lindblom (1985) inappropriate for solving g modes. The issue for these long-lived modes (due to their small imaginary components) has been addressed in Krüger, Ho & Andersson (2015) by solving a slightly different set of differential equations (see also Finn 1986). In this work we adopt the combined algorithm of Andersson et al. (1995) and Krüger et al. (2015) to compute g modes. Our code is capable of determining the real parts of mode frequencies to within a tolerance of $\sim$10 Hz. Shown in Fig. 2 are the radial displacement ξ^r for the first five g modes of a particular star.

There is a universal relation for the frequencies of f modes over a plethora of EOS for non-rotating NSs (Andersson & Kokkotas 1998) and for (rapidly-)rotating NSs (Krüger & Kokkotas 2020), which can be used to infer the eigenfrequencies of f modes by the mean

---

[2]Solutions to the perturbation equations include those of purely ingoing- and outgoing-waves, and even the hybrid waves. However, only those pulsate energy outward, i.e. purely outgoing ones, are physically realized (Price & Thorne 1969).
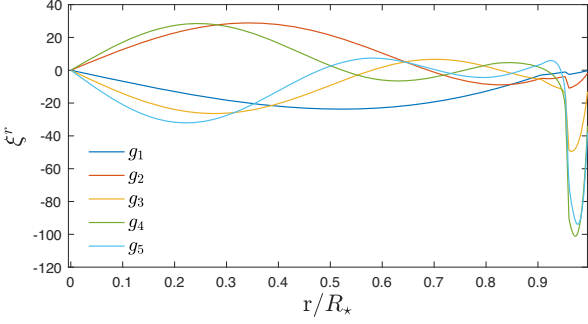
Figure 2. Normalized radial displacement ξ^r for the $n = 1 - 5$, $l = 2$, g modes of the star with EOS SLy, $M_\star = 1.27\,\mathrm{M}_\odot$, and $\delta = 0.005$.

Table 1. Fitting index ς, defined in equation (10), for leading-order g-mode frequencies as a function of δ.

EOS	APR4	SLy	WFF1	WFF2	WFF3
ς	0.231	0.378	0.148	0.212	0.465

density of the background star and vice versa (Andersson & Kokkotas 1996; Lau, Leung & Lin 2010; Völkel, Krüger & Kokkotas 2021). Similar relations have been found for other modes also (Andersson & Kokkotas 1998; Kokkotas, Apostolatos & Andersson 2001; Tsui & Leung 2005). In particular, though restricted to polytropic EOS, Xu & Lai (2017) found universal relations between the frequencies of $l = 2$, g_1 modes, and the strength of stratification (i.e. δ in our notation). Similar to Xu & Lai (2017), we find that the real parts of the eigenfrequencies are well described, as a function of δ, by

$$\mathrm{Re}[\omega_{g_1}] \propto \left(\frac{M^\varsigma}{R^{1+\varsigma}} \right) \sqrt{\delta}, \quad (10)$$

where the fitting constants ς for each EOS are listed in Table 1. For the polytropic EOS studied in Xu & Lai (2017), the corresponding constant is $\varsigma = 0.5$ – it is lower for realistic EOS.

3 BINARY EVOLUTION

We consider a close NSNS binary system with constituent masses $M_\star$ and M_{comp} for the primary and companion, respectively. The orbit is assumed to lie on the equatorial plane.[3] Each star perceives the other as a point mass to leading order, and thus we treat the companion as a point mass in the evolutionary code.[4] The relevant Hamiltonian consists of four parts (Alexander 1987; Kokkotas & Schafer 1995):

(i) The conservative orbital dynamics, for which we include up to third-order post-Newtonian (PN) corrections via the effective one-body formalism (since the equations are lengthy, we refer the reader to equation (4.28) of Damour, Jaranowski & Schäfer 2000; see also Buonanno & Damour 1999).

---

[3] In close binaries, tidal interaction aligns the stellar spins with the orbital angular momentum rapidly (Hut 1981; Zahn 2008). Therefore, it is most likely that stellar spins are almost aligned with the orbital one in the late stage of inspiralling.

[4] Higher order and finite-size effects have been looked at through the second-order gravitational self-force method (Pound 2012) and, independently, by post-Newtonian theory (Bini, Damour & Faye 2012), where the leading correction comes beyond 5 PN.

(ii) Leading order GW dissipation of respective equatorial motions, which first appear at 2.5 PN order, is encapsulated by (Schaefer 1990)

$$H_{\mathrm{react}} = \frac{2}{5} \left(p_i p_j - \frac{M_\star^2 M_{\mathrm{comp}}^2}{M_\star + M_{\mathrm{comp}}} \frac{x_i x_j}{a^3} \right) \frac{\mathrm{d}^3}{\mathrm{d}t^3} \left[x_i x_j - \frac{a^2}{3} \delta_{ij} \right], \quad (11)$$

where $x_i = (a\cos\phi, a\sin\phi)$ for $i = 1, 2$ denote the spatial coordinates of the companion (note the lack of dependence on θ because we consider equatorial motion), p_i are the associated momenta, and a is the distance between the companion and the centre of the primary ($r = 0$).

(iii) The gravitational energy that the primary absorbs via the tidal field,

$$H_{\mathrm{tid}} = \int_{\mathrm{primary}} \Phi^{\mathrm{T}} \delta\rho(\boldsymbol{x}, t) \sqrt{-g} \mathrm{d}^3 x, \quad (12)$$

where Φ^{T} denotes the tidal potential as experienced by the primary, $\delta\rho$ is the physical variation in density, and the integral is taken over the volume of the primary. We note that the tidal potential Φ^{T} is not to be confused with the metric function $\Phi(r)$. In true general relativity, the tidal potential Φ^{T} (which is promoted to a tensor) has both electric and magnetic components (Landry & Poisson 2015; Poisson & Douçot 2017; Poisson 2020) (see also Ferrari, Gualtieri & Maselli 2012; Vines & Flanagan 2013; Steinhoff et al. 2016, for the formalism of 1 PN interaction). However, the PN tidal response of NSs and the influence on the orbit evolution are insignificant except only the last few seconds of the inspiral ($\gg 100$ Hz). Therefore, we will neglect the PN tidal interaction and consider a Newtonian approximation here. As such, Φ^{T} admits a multipole expansion of the form (Press & Teukolsky 1977; see also Zahn 1977, for the case of eccentric binaries)

$$\Phi^{\mathrm{T}} = -\frac{M_{\mathrm{comp}}}{a} \left[1 + \sum_{l=2} \left(\frac{r}{a} \right)^l P_0^l \left(\cos\tilde{\phi} \sin\theta \right) \right], \quad (13)$$

which depends on the difference $\tilde{\phi} = \phi - \phi_{\mathrm{c}}$ between ϕ and the angular position of the secondary star, ϕ_{c}, as measured from the perihelion of the orbit. In general, one needs to sum over the multipolar components of Φ^{T} to complete the tidal Hamiltonian, though we specialize our attention to the $l = m = 2$ component of Φ^{T}, which is the leading order term of the potential most relevant for tidally-forced oscillations (Zahn 1977; Willems 2003). The tidal force associated with this component perturbs the primary with frequency two times the orbital frequency, $2\Omega_{\mathrm{orb}}$. In addition, $\delta\rho(\boldsymbol{x}, t)$ is induced by the small-amplitude motion ξ on the star,

$$\boldsymbol{\xi}(\boldsymbol{x}, t) = \sum_\alpha q_\alpha(t) \boldsymbol{\xi}_\alpha(\boldsymbol{x}, t), \quad (14)$$

which we have decomposed into modes ξ_α with amplitude q_α (see Section 3.1 for details). Each ξ_α, having time dependence $\mathrm{e}^{i\omega_\alpha t}$, is a solution to the eigenproblem ,

$$\mathcal{V}\boldsymbol{\xi}_\alpha = \omega_\alpha^2 \mathcal{T}\boldsymbol{\xi}_\alpha, \quad (15)$$

where $\mathcal{V}$ and $\mathcal{T}$ are appropriate potential and kinetic operators (Fuller et al. 2020). The detailed form of these potentials is crucial as one attempts to identify the impact of any perturbing forces in the problem, but is not important in building up the Hamiltonian itself, so we postpone their explicit definition until Section 5.2.

(iv) Pulsations on the primary, which are described by a harmonic-oscillators-type Hamiltonian ,

$$H_{\mathrm{osc}} = \frac{1}{2} \sum_\alpha \left(\frac{p_\alpha \bar{p}_\alpha}{M_\star R_\star^2} + M_\star R_\star^2 \omega_\alpha^2 q_\alpha \bar{q}_\alpha \right) + \mathrm{H.c.}, \quad (16)$$

which is normalized according to

$$\int_{\text{primary}} \sqrt{-g}\,\mathrm{d}^3x\,\mathrm{e}^{-2\Phi}(\rho + p)(\xi_\alpha)^\mu(\bar{\xi}_{\alpha'})_\mu = M_\star R_\star^2 \delta_{\alpha\alpha'} \tag{17}$$

for each QNM eigenfunction.[5] Here p_α are the canonical momenta associated with q_α, and the overhead bar denotes complex conjugation. Note that the momenta with Latin index are spatial ones, while those labelled by α are for pulsations. The Hermitian conjugate in equation (16) comes from the dual appearance of modes with eigenfrequency $-\bar{\omega}$ (see Section 3.1 for details). However, these are not the classic oscillators in the sense that dissipation rate of QNMs is not determined solely by the imaginary part of the eigenfrequencies, since the eigenfunctions are not real.

In summary, we work with the Hamiltonian,

$$H(t) = (H_{\text{orb}} + H_{\text{reac}} + H_{\text{osc}} + H_{\text{tid}})(t). \tag{18}$$

The orbital dynamics are then determined by numerically solving Hamilton's equations,

$$\frac{\mathrm{d}p_\alpha}{\mathrm{d}t} = -\frac{\partial H(t)}{\partial q_\alpha}, \quad \frac{\mathrm{d}q_\alpha}{\mathrm{d}t} = \frac{\partial H(t)}{\partial p_\alpha}, \tag{19a}$$

$$\frac{\mathrm{d}\bar{p}_\alpha}{\mathrm{d}t} = -\frac{\partial H(t)}{\partial \bar{q}_\alpha}, \quad \frac{\mathrm{d}\bar{q}_\alpha}{\mathrm{d}t} = \frac{\partial H(t)}{\partial \bar{p}_\alpha}, \tag{19b}$$

and

$$\frac{\mathrm{d}p_i}{\mathrm{d}t} = -\frac{\partial H(t)}{\partial x_i}, \quad \frac{\mathrm{d}x_i}{\mathrm{d}t} = \frac{\partial H(t)}{\partial p_i}, \tag{19c}$$

where we recall that x_i and p_i are defined in the sentence below equation (11).

The evolution is carried out up to the point that the orbital instability kicks in, which happens at $a \lesssim 3q^{1/3}R_\star$ (Lai, Rasio & Shapiro 1993), where q is the mass ratio M_{comp}/M of the binary. Although this point need not coincide with the separation where NSs merge, the difference is small (Lai, Rasio & Shapiro 1994b) and we effectively assume that mergers occur at $a \lesssim 3q^{1/3}R_\star$ (Lai, Rasio & Shapiro 1994a; Ho & Lai 1999; Suvorov & Kokkotas 2020).

3.1 Tidal resonances

For a spherically-symmetric (equilibrium) star, the components of the eigenfunction ξ_α can be expressed in terms of radial (W_{nl}) and tangential (V_{nl}) components, viz.

$$\xi_\alpha^r = r^{l-1}\mathrm{e}^{-\lambda}W_{nl}(r)Y_{lm}\mathrm{e}^{i\omega_\alpha t},$$
$$\xi_\alpha^\theta = -r^{l-2}V_{nl}(r)\partial_\theta Y_{lm}\mathrm{e}^{i\omega_\alpha t},$$
$$\xi_\alpha^\phi = -r^l(r\sin\theta)^{-2}V_{nl}(r)\partial_\phi Y_{lm}\mathrm{e}^{i\omega_\alpha t}, \tag{20}$$

and $\xi_\alpha^t = 0$ (Thorne & Campolattaro 1967; Lindblom & Detweiler 1983; Detweiler & Lindblom 1985). In addition, the metric perturbed

by (even parity) QNMs can be expressed in the Regge–Wheeler gauge[6] as

$$\mathrm{d}s^2 = \mathrm{d}s_{\text{eq}}^2 - \mathrm{e}^{2\Phi}r^l H_{nl}^0 Y_{lm}\mathrm{e}^{i\omega_\alpha t}\mathrm{d}t^2 - 2i\omega_\alpha r^{l+1}H_{nl}^1 Y_{lm}\mathrm{e}^{i\omega_\alpha t}\mathrm{d}t\,\mathrm{d}r$$
$$- \mathrm{e}^{2\lambda}r^l H_{nl}^0 Y_{lm}\mathrm{e}^{i\omega_\alpha t}\mathrm{d}r^2 - r^{l+2}K_{nl}Y_{lm}\mathrm{e}^{i\omega_\alpha t}\mathrm{d}\Omega^2, \tag{21}$$

where $\mathrm{d}s_{\text{eq}}^2$ is the line element of the equilibrium (1), and H_{nl}^0, H_{nl}^1, and K_{nl} characterize the metric perturbations.

Two modes whose eigenfrequencies have real parts with opposite sign but share the same imaginary parts appear in pairs (Andersson & Kokkotas 1998), and their eigenfunctions are complex conjugate to each other. The normalization (17) is satisfied for these dual modes; thus, the Hermitian conjugate part in equation (16) attributes to them. The change in the (Eulerian) density induced by pulsations is therefore

$$\delta\rho(\boldsymbol{x}, t) = \sum_\alpha \delta\rho(\boldsymbol{x}, \omega_\alpha)\mathrm{e}^{i\omega_\alpha t} + \text{H.c.}, \tag{22}$$

where the contribution of a particular mode, accompanying a Hermitian conjugate term due to the dual mode, is

$$\delta\rho(\boldsymbol{x}, \omega_\alpha) = q_\alpha\left[-\mathrm{e}^{-\Phi}\nabla_i\left((\rho + p)\mathrm{e}^\Phi \xi_\alpha^i \mathrm{e}^{-i\omega_\alpha t}\right)\right.$$
$$\left. + \left(\frac{H_{nl}^0}{2} + K_{nl}\right)(\rho + p)Y_{lm}\right], \tag{23}$$

to first order in the perturbation terms (cf. equation 8a in Detweiler & Ipser 1973). The boldface symbol denotes the spatial part of a four-vector and the divergence is taken with respect to the three-geometry of the metric (21) at a constant time t. The physical perturbation in density induced by a pair of modes reads

$$\delta\rho(\boldsymbol{x}, t) = 2\text{Re}[\overline{\delta\rho}(\boldsymbol{x}, \omega)]. \tag{24}$$

We use the complex conjugate $\overline{\delta\rho}$ in the bracket to maintain coherence with later use. The factor of 2 comes from the fact that the modes appear in pairs with frequency of ω and $-\bar{\omega}$.

Substituting $\delta\rho$ and integrating by parts, the tidal Hamiltonian can be expressed as

$$H_{\text{tid}} = 2\int_{\text{primary}}\sqrt{-g}\,\mathrm{d}^3x(\rho + p)\text{Re}\left[\overline{\delta\rho}(\boldsymbol{x}, \omega)\Phi^{\text{T}}\right]$$
$$= \int_{\text{primary}}\sqrt{-g}\,\mathrm{d}^3x(\rho + p)\text{Re}\left[(\bar{H}_{nl}^0 + 2\bar{K}_{nl})\bar{Y}_{lm}\Phi^{\text{T}}\right]$$
$$- \frac{2M_\star M_{\text{comp}}}{aR_\star}\sum_\alpha W_{lm}\left(\frac{R_\star}{a}\right)^l \text{Re}[\bar{q}_\alpha Q_\alpha \mathrm{e}^{-im\phi_c}], \tag{25}$$

containing a term resulting from the space–time distortion, which does not have a Newtonian analogy. In equation (25), W_{lm} is given by

$$W_{lm} = (-)^{(l+m)/2}\left[\frac{4\pi}{2l+1}(l+m)!(l-m)!\right]^{1/2}$$
$$\times \left[2^l\left(\frac{l+m}{2}\right)!\left(\frac{l-m}{2}\right)!\right]^{-1}, \tag{26}$$

---

[5]Eigenfunctions of QNMs, ξ_α^μ, in GR are not strictly orthogonal to each other for the coupling between the material motion to the gravitational radiation field, which extends to infinity, destroys the self-adjointness of the eigenvalue problem by a non-vanishing surface integral term from the perturbations in the space–time (see, e.g. equation 2.4 in Friedman & Schutz 1975; for the Cowling approximation case, see the last two terms of equation (16) in Detweiler & Ipser 1973). None the less, that term is small for g modes, whose dissipation time-scales are extremely long. The omission of the surface integral term hence justifies the implementation of the normalization (17), which looks similar to the Newtonian case used in, e.g. Tsang et al. (2012).

[6]Strictly speaking, this gauge assumes a fixed (l, m) and mode parity (cf. equations A9 and A11 in Thorne & Campolattaro 1967), and so performing a summation, as we do in (14), is actually mixing gauges in a formally incorrect way. Fortunately, Price & Thorne (1969) have shown that one can simply superpose the QNMs using whatever gauge for each one.

where $(-)^k = (-1)^k$ if k is an integer, but equals zero otherwise. The relativistic 'overlap integral', defined as (Press & Teukolsky 1977)

$$Q_{nl} = \frac{1}{M_\star R_\star^l} \int_{\text{primary}} \sqrt{-g} d^3 x (\rho + p) \bar{\xi}_{nll}^\mu \nabla_\mu (r^l Y_{ll}), \qquad (27)$$

is a complex, *dimensionless* number that measures the tidal coupling strength of the mode. The tidal overlap integral for the predominant effects ($l = m = 2$ component of Φ^T) reads[7]

$$Q_{n2} = \frac{1}{M_\star R_\star^2} \int_{\text{primary}} e^{\Phi+\lambda} (\rho + p) \bar{\xi}_{n22}^\mu \nabla_\mu (r^2 Y_{22}) r^2 d^3 x. \qquad (28)$$

For a binary system, the tidal force has the frequency of $2\Omega_{\text{orb}}$ (Zahn 1977), thus pulsation modes, with eigenfrequencies ω_α, would be brought into resonance when Ω_{orb} falls in the interval $[((1 - \epsilon)/2)\omega_\alpha, ((1 + \epsilon)/2)\omega_\alpha]$ (Lai 1994). In our numerical results, we find that the definition

$$\epsilon = 10 \sqrt{\frac{2\pi}{\Omega_{\text{orb}}} \frac{|\dot{a}|}{a}} \qquad (29)$$

is adequate for determining the onset and the end of resonance (see Fig. 4), which, in turn, yields the resonance duration $t_{\text{res}} \approx \epsilon \text{Re}(\omega_\alpha)$. On the other hand, the tidal field shifts the eigenfrequencies by (see also Section 5.2)

$$\delta\omega_\alpha^T = \frac{Q_{n2}}{2\omega_\alpha a^3} M_{\text{comp}}, \qquad (30)$$

where ω_α is the unperturbed eigenfrequency. This indicates that the true eigenfrequencies – which include a shift due to the tidal field – must be solved for simultaneously with the orbital evolution equations, since equation (30) depends on the (time-dependent) orbital separation a. In fact, any perturbing force will shift the pulsation spectrum because the kinetic and potential operators $\mathcal{V}$ and $\mathcal{T}$ defined in equation (15) are adjusted accordingly. In Section 5, we show how the Coriolis and Lorentz forces associated with a rotating and magnetized star may influence the spectrum.

The numerical scheme for evolving the modes of the primary is summarized in Fig. 3. We begin by evolving the binary with an initial separation of

$$a(0) = 2 \sqrt[3]{\frac{M_\star + M_{\text{comp}}}{(\text{Re}[\omega_\alpha])^2}}. \qquad (31)$$

The initial (non-resonant) mode amplitude is assumed to be zero. In Fig. 4 we show the mode amplitude for the $l = m = 2$, g_1 mode for a star with SLy EOS as a member of an equal-mass ($q = 1$) binary as a function of time. The resonance starts at orbital frequency $\nu_{\text{orb}} = \Omega_{\text{orb}}/2\pi = 43.89$ Hz (green point) and ends at 45.69 Hz (light green point) with duration of 0.29 s. The mode oscillates with amplitude $q \approx 2.4 \times 10^{-4}$ after resonance, though these oscillations decay exponentially as merger is reached.

We performed simulations for equal-mass binaries assuming the EOS APR4, SLy, and WFF1-3. We find that the maximal amplitudes of g_1 modes of the primary obey the following approximate relations :

$$q_{\alpha,\text{max}}(\omega_\alpha M_\star)^{5/6} \simeq (0.1092 \pm 0.0208) Q_{12}, \qquad (32)$$

where the error is given by 1σ confidence level of least-squares fitting. The analytic equation of the maximum mode amplitude under

---

[7]Note that this expression differs from that used by Yoshida & Eriguchi (1999). These latter authors ignored the pressure contribution in addition to the inertial mass in their expression.
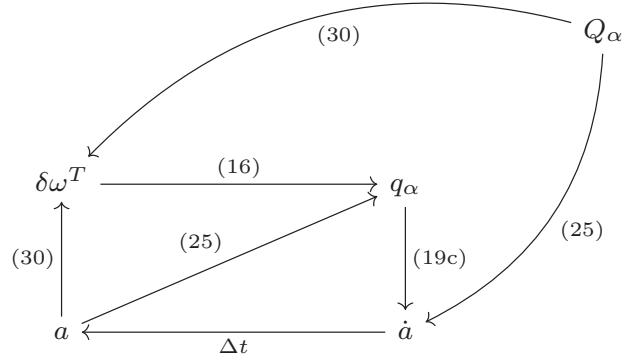
Figure 3. The numerical scheme used in this paper to evolve the modes of the primary. The only time-independent quantities are the tidal overlap integrals Q_α on the upper right, while the rest are iteratively solved for. Starting from the separation $a(t)$, the strength of tidal field by the companion of a specific binary is decided and gives rise to certain shift in eigenfrequencies of QNMs (equation 30), which depends also on the tidal coupling strength of each QNM Q_α. Consequently, total eigenfrequencies $\omega_\alpha + \delta\omega_\alpha^T$ fixes the Hamiltonian of QNMs (equation 16), which is solved to update mode amplitudes. Next, the change rate of the separation $\dot{a}$ is influenced by the amplitude of excited pulsations and the tidal coupling strength Q_α, and infers the separation at the next moment $a(t + \Delta t)$ for the time-step Δt. Then the cycle runs again until $a \lesssim 3R_\star$ (Ho & Lai 1999; Suvorov & Kokkotas 2020). Each arrow stands for a deduction via the relation labelled beside it.
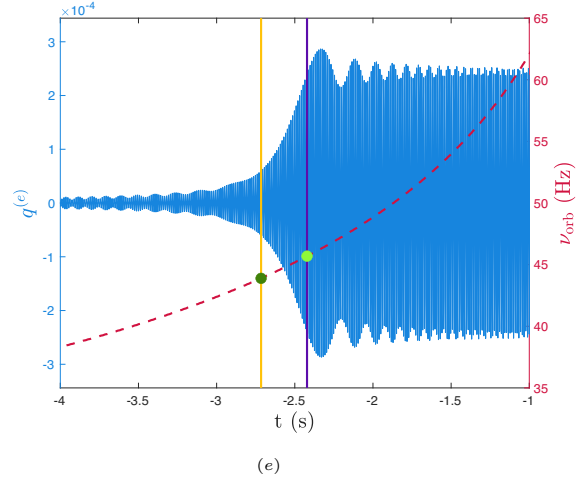

Figure 4. The amplitude $q^{(e)}$ (blue; left y-axis) of the $l = m = 2$, g_1 mode, whose unperturbed frequency is 89.25 Hz, and the orbital frequency (red; right y-axis) as functions of time. The horizontal axis records the time prior to an equal-mass NS–NS coalescence, which is achieved once the separation decays to $a \lesssim 3R_\star$ (Ho & Lai 1999; Suvorov & Kokkotas 2020). The yellow and the purple lines mark the beginning and the end of the resonance, respectively; the corresponding orbital frequencies are 43.89 and 45.69 Hz, marked by solid green points. We have taken an equal-mass binary with the SLy EOS with $M_\star = 1.27 \, M_\odot = M_{\text{comp}}$ and $R_\star = 11.78$ km. The radial displacement ξ^r of the first five g modes are shown in Fig. 2.

the stationary phase approximation suggests a slope of $\pi/32 \simeq 0.0982$ (cf. equation 6.3 in Lai 1994), which agrees our result to within the stated confidence level.

Tidal effects accelerate the merger because orbital energy leaks into the QNMs (Kokkotas & Schafer 1995; Vick & Lai 2019), especially the f modes, whose coupling strengths are typically a few tenths. For modes with coupling strengths $Q \lesssim 0.01$, the effects on the orbital evolution are negligible. In Fig. 5, we present the separation of
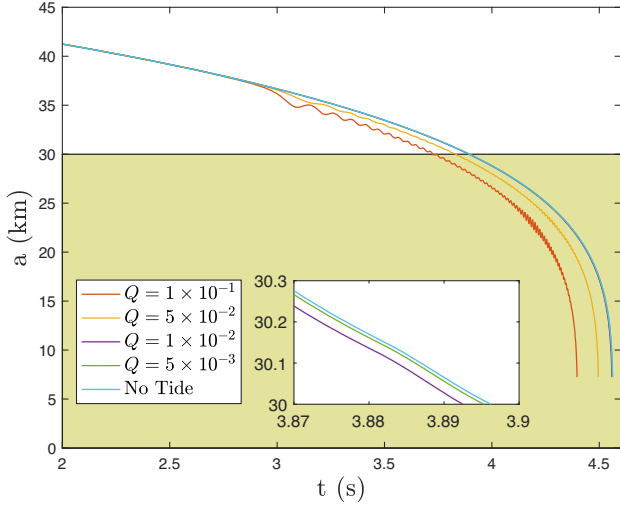
Figure 5. Binary separation with various tidal overlaps as a function of time. The maximal disagreement between $Q = 0.01$ and the case without tidal effect is $\lesssim 0.01$ s and is smaller for smaller tidal overlaps. Shaded area, where $a \lesssim 3R_\star$ (Ho & Lai 1999; Suvorov & Kokkotas 2020), marks the stage after the merger, which thus is not the virtual evolution. We have taken $M_\star = 1.4\,\mathrm{M_\odot} = M_{\mathrm{comp}}$ and $R_\star = 10$ km; hence, the collapse happens when the separation is around 30 km. The frequency of the resonant mode is 100 Hz. This Figure does not use any particular EOS.

an equal-mass binary with $M_\star = 1.4\,\mathrm{M_\odot} = M_{\mathrm{comp}}$ and $R_\star = 10$ km for four different strengths of tidal overlap Q as functions of time, together with an evolution on which the tidal effects are absent. As such, one can observe that for $Q \lesssim 0.01$ the tidal effect on the evolution is quite small. Given that the typical coupling strengths of a g mode are both much smaller than 0.01, the effect in this case of the g-mode resonances on the orbital evolution are insignificant relative to measurement uncertainties in the timing of GWs and gamma-ray-bursts.

4 MAGNETOHYDRODYNAMICS

Having explored the effect of the g modes on the orbital evolution, we now turn to the influence of magnetic fields. In this work, we treat stars as perfect conductors over which relativistic magnetic fields are constructed. Perturbed magnetic fields generate Lorentz forces according to the Faraday induction equation (Section 4.2), which tunes the eigenfrequencies of QNMs through back-reaction (Section 5.1). In the event that a crustal yielding occurs on a magnetized star, the release of fracture energy may generate flares, such as precursors of short gamma-ray bursts. In general, perturbed magnetic fields would induce electric fields, accelerating charged particle and thermalizing the electromagnetic emission; however, if the magnetic field is strong enough [$\gg 10^{13}$ G, i.e. magnetar-level (Duncan & Thompson 1992)], the energy propagates along field lines as Alfvén waves (Tsang et al. 2012). The non-thermal properties of precursors thus support the possibility that at least one NS is a highly magnetized star in those events (Suvorov & Kokkotas 2020). In any case, timing and the spectral properties of precursor will be examined in Paper II as an application of the formalism developed here.

4.1 Magnetic field structure

The Viral theorem (Chandrasekhar & Fermi 1953) sets an upper limit to the magnetic field strength for NSs of the order of $\sim 10^{18}$ G

(Lai 2001; Lattimer & Prakash 2007; Reisenegger 2009). Even for most magnetars, the (surface dipole) magnetic field strength is much smaller than this extreme, implying that the gravitational binding energy exceeds the magnetic energy by several orders of magnitude (Sotani et al. 2007; Akgün et al. 2013). One may therefore treat the magnetic field as a perturbation over a spherically symmetric background profile (1), in the style of Ciolfi et al. (2009) and Mastrano et al. (2011, 2015).

We introduce the electromagnetic four-potential A_μ, which defines the Faraday tensor

$$F_{\mu\nu} = \nabla_\nu A_\mu - \nabla_\mu A_\nu, \tag{33}$$

where each A_μ is a function of r and θ only. Maxwell's equations for the electromagnetic field are

$$F^{\mu\nu}_{;\nu} = 4\pi J^\mu, \qquad \nabla_{[\alpha} F_{\beta\gamma]} = 0, \tag{34}$$

for four-current J^μ [effectively defined by the first of equations. (34)]. The Lorentz force is then given by $F^\mu_L = F^{\mu\nu} J_\nu$. The ideal MHD condition of vanishing electric field, defined by

$$E_\mu = F_{\mu\nu} u^\nu, \tag{35}$$

for a static and non-rotating star (i.e. $u^\mu = \mathrm{e}^{-\Phi} \partial_t$), returns the condition $A_t = 0$. We have residual gauge freedom, which allows us to pick $A_\theta = 0$ (Glampedakis & Lasky 2016). Setting $A_r = B_\star \mathrm{e}^{\lambda - \Phi} \Sigma$ and $A_\phi = B_\star \psi$, it can be shown that Maxwell's equations are solved exactly for (Ciolfi et al. 2009)

$$\Sigma(r, \theta) = \int \mathrm{d}\theta \zeta(\psi) \frac{\psi(r, \theta)}{\sin\theta}, \tag{36}$$

for some ζ, which is an arbitrary function of the stream function ψ and effectively defines the azimuthal (toroidal) component B_ϕ, effectively generalizing the Chandrasekhar (Helmholtz) decomposition in flat space (Chandrasekhar 1956; Mastrano et al. 2011). Here $B_\star$ sets the characteristic field strength.

The magnetic four-field has covariant components :

$$B_\mu = \frac{1}{2} \epsilon_{\mu\nu\sigma\eta} u^\nu F^{\sigma\eta}, \tag{37}$$

where ϵ denotes the Levi–Civita symbol. Using the above expression for A_μ, the contravariant components B^μ can be readily evaluated, and we find

$$B^\mu = B_\star \left(0, \frac{\mathrm{e}^{-\lambda}}{r^2 \sin\theta} \frac{\partial \psi}{\partial \theta}, -\frac{\mathrm{e}^{-\lambda}}{r^2 \sin\theta} \frac{\partial \psi}{\partial r}, -\frac{\zeta(\psi) \psi \mathrm{e}^{-\Phi}}{r^2 \sin^2\theta} \right). \tag{38}$$

The function ψ can now be expanded as a sum of multipoles. For simplicity, we take a dipole field with polynomial radial component (which generalizes the Newtonian description in Mastrano et al. 2011), i.e.

$$\psi(r, \theta) = f(r) \sin^2\theta, \tag{39}$$

with $f(r) = a_1 r^2 + a_2 r^4 + a_3 r^6$, where a_i are to be constrained by appropriate boundary conditions. In particular, we impose that (i) the field matches to a force-free dipole outside of the star ($r > R_\star$), and (ii) there are no surface-currents ($J^\mu|_{r=R_\star} = 0$). This leads to *four* constraints, which are that the three components (38) are continuous at the boundary ∂V of the star, and that the four-current vanishes there (which only has one non-trivial component, J_ϕ, for an axisymmetric field). One of these is trivially satisfied by demanding that ζ vanishes on the surface, which we achieve, as in Mastrano et al. (2011), by setting

$$\zeta(\psi)\psi = -\left[\frac{E^p (1 - \Lambda)}{E^t \Lambda} \right]^{1/2} \frac{(\psi - \psi_c)^2}{R_\star^3}, \tag{40}$$

when $\psi \geq \psi_c$, and ζ is zero otherwise. Here ψ_c is the critical value of the streamfunction, defined as the value of the last poloidal field line that closes within the star, thus the toroidal component is confined to the region of closed poloidal field lines. The quantity Λ measures the ratio of poloidal and toroidal magnetic energies; typically $\Lambda \ll 1$ for a stable configuration (Braithwaite 2009; Akgün et al. 2013). For the above choices, we find

$$\psi_c = -\frac{3R_\star^3 \sin^2 \theta}{8M_\star^3}\left[2M_\star(M_\star + R_\star) + R_\star^2 \log\left(1 - \frac{2M_\star}{R_\star}\right)\right]. \quad (41)$$

The energy stored in the *internal* magnetic field of the static equilibrium is (see, e.g. equation 41 in Ciolfi et al. 2009)

$$E = 2\int_{\text{primary}} \sqrt{-g}\,d^3x\, u_\mu u_\nu T^{\mu\nu} = \frac{1}{4\pi}\int_{\text{primary}} \sqrt{-g}\,d^3x\, B^2, \quad (42)$$

where $T^{\mu\nu}$ is the magnetic stress-energy tensor

$$T^{\mu\nu} = \frac{B^2}{4\pi}\left(u^\mu u^\nu + \frac{1}{2}g^{\mu\nu}\right) - \frac{B^\mu B^\nu}{4\pi}, \quad (43)$$

with $B^2 = B^\mu B_\mu$. For the dipolar field (38) considered here, the poloidal and toroidal energies are

$$E^p = \frac{B_\star^2}{4\pi}\int_{\text{primary}} \sqrt{-g}\,d^3x\left[\left(\frac{\partial_\theta \psi}{r^2 \sin\theta}\right)^2 + \left(\frac{e^{-\lambda}\partial_r \psi}{r \sin\theta}\right)^2\right], \quad (44)$$

and

$$E^t = \frac{B_\star^2}{8\pi}\int_{\psi \geq \psi_c} \sqrt{-g}\,d^3x\left(\frac{\zeta(\psi)\psi e^{-\Phi}}{r \sin\theta}\right)^2, \quad (45)$$

respectively.

The force-free dipole outside of the star is found by setting $F_L^\mu = 0$ for $r > R_\star$. This leads to (Wasserman & Shapiro 1983)

$$\psi_{\text{ext}} = -\frac{3R_\star^3 \sin^2 \theta}{8M_\star^3}\left[2M_\star(r + M_\star) + r^2 \log\left(1 - \frac{2M_\star}{r}\right)\right], \quad (46)$$

where we note that, outside of the star, the geometry is Schwarzschild, i.e.

$$\Phi(r > R_\star) = \frac{1}{2}\log\left(1 - \frac{2M}{r}\right) \text{ and } \lambda(r > R_\star) = -\Phi. \quad (47)$$

It is not hard to prove (use L'Hopital's rule) that, in the limit $M_\star \to 0$, ψ_{ext} reduces to the standard force-free dipole of Newtonian theory, $\psi \sim \sin^2\theta/r$. Finally, imposing the conditions (i) and (ii) discussed above leads to

$$a_1 = -\frac{3R_\star^3}{8M_\star^3}\left[\log\left(1 - \frac{2M_\star}{R_\star}\right) \right.$$
$$\left. + \frac{M_\star(24M_\star^3 - 9M_\star^2 R_\star - 6M_\star R_\star^2 + 2R_\star^3)}{R_\star^2(R_\star - 2M_\star)^2}\right], \quad (48a)$$

$$a_2 = \frac{3(12M_\star - 7R_\star)}{4R_\star(R_\star - 2M_\star)^2}, \quad (48b)$$

and lastly

$$a_3 = \frac{3(5R_\star - 8M_\star)}{8R_\star^3(R_\star - 2M_\star)^2}. \quad (48c)$$

The above therefore completely defines the general-relativistic generalization of the Mastrano et al. (2011) mixed poloidal-toroidal field.

The magnetic field introduces a frequency shift in the spectrum of the star depending on the values $B_\star$ and Λ, defining the characteristic poloidal and toroidal strengths. To better understand the magnetic field, we transform the contravariant components of four-field B^μ
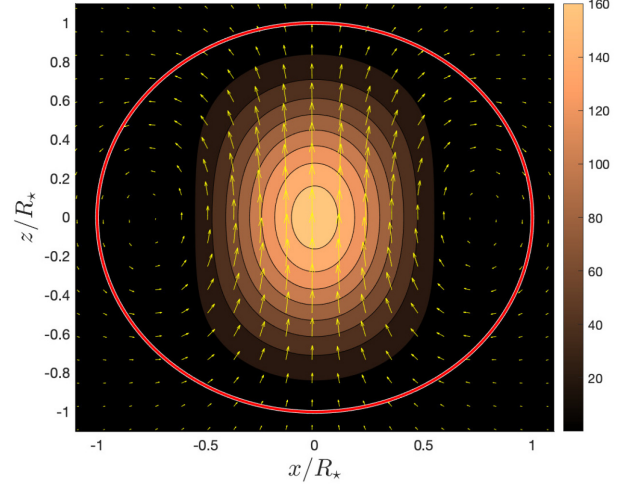

Figure 6. Field lines for the background magnetic field $\boldsymbol{B}$ with $\Lambda = 1$. The red rigid line marks the surface of the equilibrium star; the scale is given in unit of $B_\star$ for which brighter shades indicate stronger field strength.

into the *Newtonian-like* components, denoted by a overhead tilde, through (cf. equation 4.8.5 in Weinberg 1972)

$$\tilde{B}_a = \sqrt{g_{aa}}B^a, \quad (49)$$

and we show the cross-section in Fig. 6, which is the whole picture of the magnetic field if the field is purely poloidal.

4.2 Perturbed Lorentz force and Faraday equations

We now study the backreaction on to the magnetic fields induced by the modes, which results in the frequency modulation 5. In this section, we ignore the space–time variation of QNMs *from magnetic fields* in the perturbation equations ($\delta g_{\mu\nu}^{\text{mag}} = 0$). Nonetheless we note that the difference between our approximation and the Cowling one is that we take the first-order space–time perturbations into account, viz. space–time perturbations are involved in determining the mode frequency of the stars, and only the higher order 'magnetic-back-reaction' effects are disposed of. In this sense, our results are expected to be more accurate than those which adopt the Cowling approximation.

Following the derivation in Sotani et al. (2007) (see also Papadopoulos & Esposito 1982), the projection of the equation of motion on to the hypersurface orthogonal to u^μ,

$$h_\eta^\mu \nabla_\nu T^{\eta\nu} = 0, \quad (50)$$

gives

$$\left(\rho + p + \frac{B^2}{4\pi}\right)u^\nu \nabla_\nu u^\mu = -h^{\mu\nu}\nabla_\nu\left(p + \frac{B^2}{8\pi}\right)$$
$$+ h_\eta^\mu \nabla_\nu\left(\frac{B^\eta B^\nu}{4\pi}\right), \quad (51)$$

where the projection operator $h^{\mu\nu} = g^{\mu\nu} + u^\mu u^\nu$. The Lagrangian four-displacement ξ^μ is related to the perturbed velocity through the Lie derivative (see, e.g. equation 34 of Friedman 1978),

$$\delta u^\mu = h_\nu^\mu \mathcal{L}_{\boldsymbol{u}}\xi^\nu. \quad (52)$$

In the simple case of a static fluid ($u^\mu = e^{-\Phi}\partial_t$), we find $\delta u^i = i\omega_\alpha e^{-\Phi}\xi^i$ for a certain QNM. After linearizing the equation of motion

(51) and utilizing relation (52), the perturbing Lorentz force reads

$$
\delta F_B^\mu = \frac{i\omega_\alpha e^{-\Phi}}{4\pi}\left[B^2\left(\nabla_t(\xi^\mu e^{-\Phi}) + \xi^\nu \nabla_\nu u^\mu\right) \right.
$$
$$
+ \frac{u^\mu \xi^\nu + u^\nu \xi^\mu}{2}\nabla_\nu(B^2) - (u^\mu \xi_\eta e^{2\Phi} + \xi^\mu u_\eta)\nabla_\nu(B^\eta B^\nu) \Big]
$$
$$
- \frac{1}{4\pi}h_\eta^\mu \nabla_\nu(B^\eta \delta B^\nu + \delta B^\eta B^\nu) + \frac{1}{4\pi}h^{\mu\nu}\nabla_\nu(B_\eta \delta B^\eta)
$$
$$
+ \frac{1}{2\pi}B_\eta \delta B^\eta u^\nu \nabla_\nu u^\mu, \tag{53}
$$

while the perturbed magnetic field δB^μ can be determined by solving the linearized induction equation (Sotani et al. 2007)

$$
\nabla_t \delta B^\mu = i\omega_\alpha\big[-\xi^\nu \partial_\nu B^\mu - \xi^\nu \Gamma^\mu_{\nu\eta}B^\eta - u^\mu \xi_\nu B^\eta \partial_\eta u^\nu
$$
$$
+ e^\Phi B^\nu \nabla_\nu(e^{-\Phi}\xi^\mu) - e^\Phi B^\mu \partial_\nu(e^{-\Phi}\xi^\nu) - B^\mu \Gamma^\nu_{\nu\eta}\xi^\eta
$$
$$
+ u^\mu B^\nu i\omega_\alpha e^{-\Phi}\xi_\nu + u^\mu B^\nu \xi^\eta(\partial_\eta u_\nu + \Gamma^t_{\nu\eta}e^\Phi)
$$
$$
- u^\mu B^\nu \Gamma^\eta_{\nu t}\xi_\eta + \xi^\mu B^r \Phi'\big] + \delta B^r u^\mu \Phi' e^\Phi. \tag{54}
$$

For the magnetic field given by equation (38), the induction equation gives

$$
\frac{\partial}{\partial t}\delta B^\mu = i\omega_\alpha\big[-\xi^r \partial_r B^\mu - \xi^\theta \partial_\theta B^\mu + B^\nu \partial_\nu \xi^\mu + B^\mu \Phi'\xi^r
$$
$$
- B^\mu \partial_\nu \xi^\nu - B^\mu \Gamma^\nu_{\nu\eta}\xi^\eta + u^\mu B^\nu i\omega_\alpha e^{-\Phi}\xi_\nu\big]
$$
$$
+ \delta B^r u^\mu e^\Phi \Phi' - \Gamma^\mu_{t\nu}\delta B^\nu. \tag{55}
$$

Since some terms only appear in the temporal component of the first-derivative of δB^μ, one can make the equations more concise by separating the temporal component from the spatial, viz.

$$
\frac{\partial}{\partial t}\delta B^t = -\omega_\alpha^2 e^{-2\Phi}B^\nu \xi_\nu, \tag{56a}
$$
$$
\frac{\partial}{\partial t}\delta B^i = -i\omega_\alpha\Big[(\xi^r \partial_r + \xi^\theta \partial_\theta - \Phi'\xi^r + \partial_\nu \xi^\nu + \xi^\nu \partial_\nu \ln\sqrt{|g|})B^i
$$
$$
- B^j \partial_j \xi^i\Big]. \tag{56b}
$$

Accordingly, one can integrate the above equations to find

$$
\delta B^t = i\omega_\alpha e^{-2\Phi}B^a \xi_a, \tag{57a}
$$
$$
\delta B^i = -\Big[\Big(\xi^r \partial_r + \xi^\theta \partial_\theta - \Phi'\xi^r + \partial_a \xi^a
$$
$$
+ \xi^r\Big(\Phi' + \lambda' + \frac{2}{r}\Big) + \frac{\xi^\theta}{\tan\theta}\Big)B^i - B^j \partial_j \xi^i\Big]. \tag{57b}
$$

Expressions (57) will be used to define the perturbing Lorentz force in Section 5.1.

Though it is not considered in this work, we would like to point out the possibility that NSs as a member of a binary may be cold enough that they contain superconducting matters, which influences the magnetic properties of the star (Lander 2013) and any resulting GWs (Suvorov 2021). For example, the force induced from the field perturbation has different influences to the Lorentz force, and the induction equation is also altered due to the altered nature of Ohmic and ambipolar dissipation (Graber et al. 2015). On top of that, superfluidity increases the frequencies of *g* modes, e.g. Yu & Weinberg (2017) found that the frequency of the $n = 1$, g_1 mode is of the order of a few hundred Hz (even up to 700 Hz) for a particular EOS with $M = 1.4\,\mathrm{M_\odot}$ (see their fig. 4). Adding that the overlap integral is found to be of the same order as the case where the superfluid is absent (see their fig. 5), we expect a smaller amplitude

for the g_1 mode due to its shorter resonance time-scale. Although the inclusion of superfluidity brings higher order modes into play, those overtones typically have a much weaker overlap integral (with respect to the normal fluid case). It may thus not be very plausible that these overtones can account for tidally-driven crustal failure.

5 MODE FREQUENCY MODULATIONS

The introduction of a perturbing force δF^μ into the Euler equations (5) leads to a modulation $\delta\omega$ in mode frequencies, while eigenfunctions are left unchanged to leading order (Unno et al. 1979; Bi, Liao & Wang 2003; Suvorov & Kokkotas 2020). The restriction of the Euler equation (5) of the unperturbed equilibrium to the hypersurface orthogonal to u^μ, i.e. $h_{\mu\nu}\nabla_\eta T^{\eta\nu} = 0$, gives

$$
(\rho + p)u^\nu \nabla_\nu u^\mu = -h^{\mu\nu}\nabla_\nu p, \tag{58}
$$

from which and equation (52), one can derive the linearized equation

$$
(\rho + p)e^{-2\Phi}\omega^2 \xi^\mu = (\delta\rho + \delta p)u^\nu \nabla_\nu u^\mu + h^{\mu\nu}\nabla_\nu \delta p
$$
$$
+ i\omega e^{-\Phi}[(\rho + p)\nabla_\nu u^\mu + u^\mu \nabla_\nu p]\xi^\nu
$$
$$
+ i\omega e^{-\Phi}\xi^\mu u^\nu \nabla_\nu p. \tag{59}
$$

The left- and right-hand sides give, respectively, the kinetic operator $\mathcal{T}$ and the potential operator $\mathcal{V}$ that are defined in equation (15). This equation, with appropriate boundary conditions, forms an eigenvalue problem for ω_α^2.

For an mode with unperturbed frequency ω_α, the inclusion of a perturbing force δF^μ on the right-hand side of (59), its eigenvalues would be amended accordingly by $\delta\omega_\alpha$. Substituting $\omega = \omega_\alpha + \delta\omega_\alpha$ and focusing on the leading order perturbation terms, (59) gives

$$
2(\rho + p)e^{-2\Phi}\omega_\alpha \xi^\mu \delta\omega_\alpha = \delta F^\mu, \tag{60}
$$

from which the frequency shift,

$$
\delta\omega_\alpha = \frac{1}{2\omega_\alpha}\frac{\int_{\mathrm{primary}}\delta F_\mu \bar{\xi}^\mu \sqrt{-g}\mathrm{d}^3 x}{\int_{\mathrm{primary}}(\rho + p)e^{-2\Phi}\xi^\mu \bar{\xi}_\mu \sqrt{-g}\mathrm{d}^3 x}, \tag{61}
$$

can be obtained. A similar derivation in the Newtonian case can be found in Unno et al. (1979). Equation (61) is numerically evaluated for some particular choices of δF^μ.

5.1 Magnetic field

As $\delta\boldsymbol{F}$ is given by the Lorentz force, (53) and (61) yield the expression of the correction in the frequency for a general magnetic field, which, after substituting the magnetic field as defined in equation (38) and adopting the normalization (17), becomes

$$
\delta\omega_\alpha^B = \frac{(M_\star R_\star^2)^{-1}}{8\pi\omega_\alpha}\int_{\mathrm{primary}}\sqrt{-g}\mathrm{d}^3 x\big[-\omega_\alpha^2 B^2 \xi^\mu \bar{\xi}_\mu e^{-2\Phi}
$$
$$
+ 2B_\mu \delta B^\mu \bar{\xi}^r \Phi' - \bar{\xi}_\mu \nabla_\nu(B^\mu \delta B^\nu + B^\nu \delta B^\mu)
$$
$$
+ \bar{\xi}^\nu \nabla_\nu(B_\mu \delta B^\mu)\big]. \tag{62}
$$

In Fig. 7, we plot the mode frequency shifts for the $l = 2$, g_1, and g_2 modes ($n = 2$) with some fixed stellar parameters and EOS as functions of the poloidal-to-toroidal strength Λ (top panel). The range of Λ is chosen broadly compared to the ratio for a stable magnetic field configuration (shaded area), which is $10^{-3} \lesssim \Lambda \lesssim 0.3$ (Akgün et al. 2013; Herbrik & Kokkotas 2017). The stability examined by the energy variation method gives the constraint

$$
\tilde{B}^\phi \lesssim 10^{17}\sqrt{B_{15}}\left(\frac{\delta}{0.01}\right)\mathrm{G}, \tag{63}
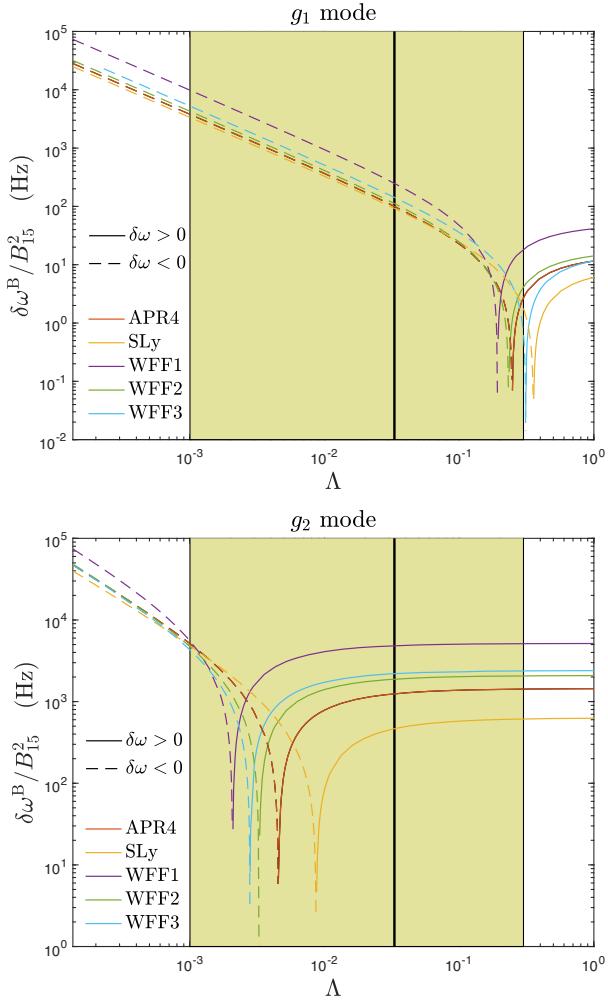$$

Figure 7. Eigenfrequency shifts $\delta\omega^B$ for the $l = 2$, $g_1 -$ (top panel) and g_2 modes (bottom panel) due to the magnetic field as functions of the poloidal-to-toroidal field-strength ratio Λ. The shaded areas represent the range of Λ for which the magnetic field is stable (Akgün et al. 2013). The black solid lines mark the ratio $\Lambda = 0.033$, which gives the maximal toroidal field strength for $B_\star = 10^{15}$ G inside the star (equation 63). We have used $\delta = 0.005$ and $\rho_c = 9 \times 10^{14}$ g cm^{-3} for EOS APR, SLy, and WFF1-3, whose masses are 1.21, 1.27, 0.86, 1.14, and 1.04 M$_\odot$, respectively.

on the toroidal strength, which implies $\Lambda \gtrsim 0.033$ (black line) for a magnetar-level surface field strength $B_\star \sim 10^{15}$G. This constraint on the strength of toroidal component becomes loose for larger δ (Akgün et al. 2013; Herbrik & Kokkotas 2017). On the other hand, we find that the Virial limit on the field strength of $\sim 10^{18}$ G inside the star (Lai 2001; Lattimer & Prakash 2007; Reisenegger 2009) corresponds to $\Lambda \gtrsim 5 \times 10^{-4}$, which is a weaker constraint than that coming from stability considerations. Unless $\Lambda \ll 1$, magnetic fields of the order $\gtrsim 10^{15}$ G are needed to noticeably shift the g_1-mode frequencies for any EOS, though marginally weaker (though still strong) fields of order $\gtrsim 10^{14}$ G can significantly adjust the g_2-mode frequencies. Given that the g_1 mode typically oscillates at ~ 100 Hz, the (rotating frame) frequency becomes negative when the ratio Λ is less than the value (black line) that implies the maximal toroidal strength for $B_\star = 10^{15}$G, indicating the onset of instability. Moreover, the frequency shifts for overtones ($n > 1$) are less sensitive to Λ than g_1 modes, resulting from nodes of displacements in the region where the toroidal component of magnetic field is non-trivial. The coupling
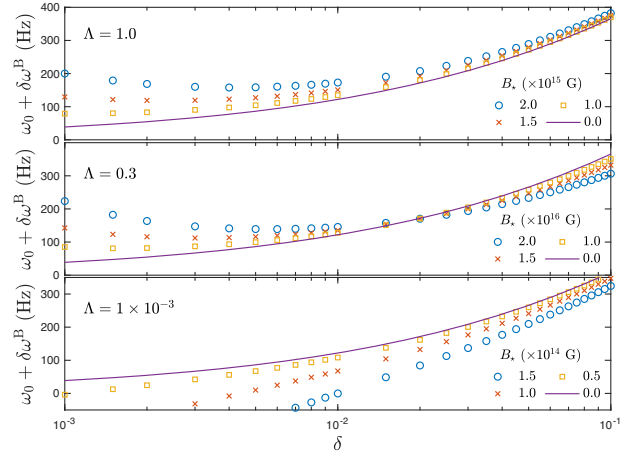

Figure 8. g_1-mode frequencies: the purple continuous line is for unperturbed star, while the rest for magnetized ones with different strengths of the magnetic field $B_\star$ as a function of δ. We set $\Lambda = 1.0$ (top panel), $\Lambda = 0.3$ (middle panel), and $\Lambda = 10^{-3}$ (bottom panel). The background star is constructed by EOS APR4 and has the central density of 8×10^{14} g cm^{-3}.

between these modes and the structure of magnetic field is thus more tenuous. For g_2 modes, a toroidal-to-poloidal ratio Λ of $\lesssim 0.01$ is needed in order that $\delta\omega^B$ becomes negative; and the shifts are always positive (for stable values of Λ) for g_3 modes, though not shown here. Fig. 8 shows modified mode frequencies of g_1 modes of a specific star for the cases $\Lambda = 1.0$ (top panel), 0.3 (middle panel), and 10^{-3} (bottom panels), for various values of $B_\star$, as functions of δ. There ω_0 denotes the unperturbed frequency. As $\delta \lesssim 0.01$, the absolute values of frequency corrections increase as the stratification weakens, i.e. δ is lower, in that unperturbed frequencies in the denominator of the right-hand side of (62) converges to zero faster than the numerator.

It is noticeable that the corrections are more severe for less compact stars when a purely poloidal ($\Lambda = 1$) field is considered, as shown in Fig. 9. For instance, defining the compactness as $\mathcal{C} = M_{1.4}/R_{10}$, we see that for $B_\star = 10^{15}$G, $\delta = 0.005$, and EOS SLy, the correction for the g_1 mode is $\delta\omega^B = 42.40$Hz for the model with $\mathcal{C} = 0.461$, while it is $\delta\omega^B = 20.32$Hz for the model with $\mathcal{C} = 0.729$. Additionally, we find fitting relations for the effect of magnetic field on the g_1 modes as

$$\delta\omega^B \approx B_{15}^2 e^{(c_1 \ln \delta + c_0)(d_1 \mathcal{C} + d_0)} \text{ Hz.} \tag{64a}$$

The fitting coefficients for different EOS are summarized in Table 2.

5.2 Tidal forces

The tidal force generated by the companion, as exerted on the primary, reads

$$\delta F_\mu^T = \frac{M_{comp}}{a^3}(\rho + p)\nabla_\mu(r^2 Y_{22}). \tag{65}$$

The equation for the frequency shift driven by this force is found to be

$$\delta\omega_\alpha^T = \frac{M_{comp}}{2\omega_\alpha a^3} \frac{\int_{primary}(\rho + p)\nabla_\mu \Phi^T \bar{\xi}^\mu \sqrt{-g}d^3x}{\int_{primary}(\rho + p)e^{-2\Phi}\xi^\mu \bar{\xi}_\mu \sqrt{-g}d^3x}. \tag{66}$$

This form is used in equation (30). The tidal force modifies the eigenfrequencies of QNMs via the interaction mediated by the pressure (hence density) variation. Consequently, it leads to minute
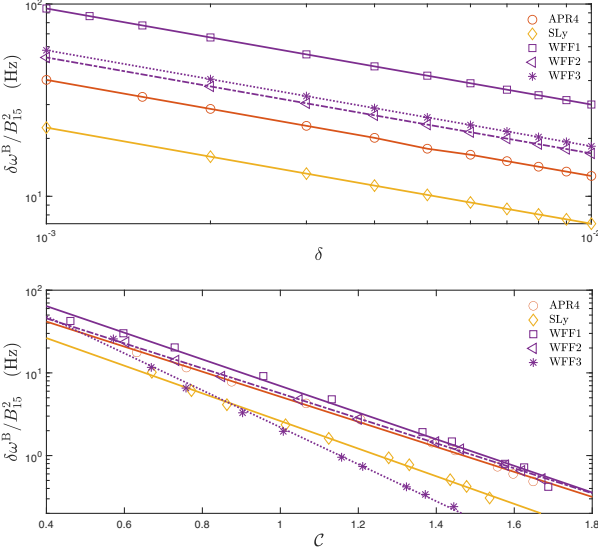
Figure 9. Magnetic-driven modifications in eigenfrequencies of $l = 2$, g_1 mode as functions of stratification δ (top panel), and the compactness $\mathcal{C}$ (bottom panel), respectively. The markers in the upper panel are the numerical results for the star of each EOS that has central density of $8 \times 10^{14}\,\mathrm{g\,cm^{-3}}$, while the markers in the bottom panel represent the stars described in Fig. 1 with fixed $\delta = 0.005$. We have taken $B_\star = 10^{15}$ G and EOSs APR4, SLy, and WFF1-3 are included. In both plots, the rigid lines are the fitting results of corrections in magnetic frequencies for each EOSs.

Table 2. Coefficients of the fitting functions (64a) for the magnetic-driven frequency modifications.

	APR4	SLy	WFF1	WFF2	WFF3
c_1	-0.493	-0.492	-0.498	-0.494	-0.495
c_0	0.279	-0.289	1.112	0.547	0.624
d_1	-3.489	-3.848	-3.707	-3.480	-5.150
d_0	5.126	4.811	5.645	5.213	5.937

frequency corrections (~ 0.01 per cent) for g modes since g modes only perturb the pressure profile slightly.

5.3 Rotation

We treat the rotation of the star as a perturbation over the non-spinning equilibrium, since the Coriolis force is proportional to the square of the angular velocity, and thus a slow perturbation, to linear order, does not induce any hydromagnetic changes to the background structure (Hartle 1967). We also omit the spin–orbit interaction. A (uniform) rotation Ω introduces a $g_{t\phi}$ component to the metric, causing frame dragging. When a slow rotation is considered, this effect is small and we therefore ignore it in this work. On top of the metric corrections, rotation also introduces the axial component ,

$$u^\mu_{\mathrm{rot}} = \Omega e^{-\Phi} \partial_\phi, \tag{67}$$

to the four-velocity, when we are working in the inertial frame. The axial velocity u^μ_{rot} adds an extra term to equation (52), resulting in

$$\delta u^\mu = i(\omega_\alpha + m\Omega)e^{-\Phi}\xi^\mu, \tag{68}$$

and thus leads to a perturbing force,

$$\delta F^r_R = 2(\rho + p)e^{-2\Phi}\omega_\alpha\Omega(m\xi^r - ir\,e^{-2\lambda}\sin^2\theta\xi^\phi), \tag{69a}$$
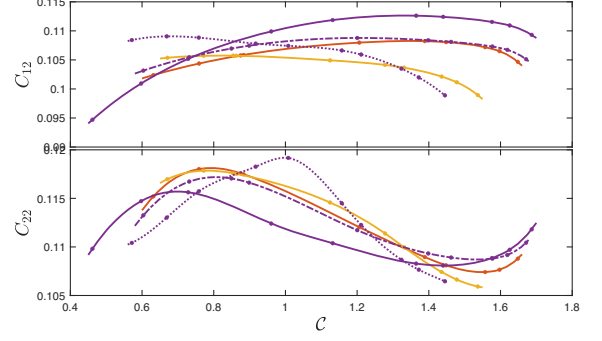

Figure 10. Coefficients C_{12} for g_1 modes (top panel), C_{22} for g_2 modes as functions of compactness $\mathcal{C}$ assuming EOS APR4 (red curves), SLy (yellow curves), and WFF1-3 (purple solid, dashed, and dotted curves, respectively). We fix $\delta = 0.005$. Markers on each curve are models pointed out in Fig. 1.

$$\delta F^\theta_R = 2(\rho + p)e^{-2\Phi}\omega_\alpha\Omega(m\xi^\theta + i\sin\theta\cos\theta\xi^\phi), \tag{69b}$$

$$\delta F^\phi_R = 2(\rho + p)e^{-2\Phi}\omega_\alpha\Omega\left(m\xi^\phi - i\frac{\xi^r}{r} - 2i\cot\theta\xi^\theta\right). \tag{69c}$$

Therefore, the relativistic leading order rotational corrections in the mode frequencies having the expression

$$\delta\omega^R_\alpha = -m\Omega(1 - C_{nl}), \tag{70}$$

with

$$C_{nl} = \frac{1}{M_\star R_\star^2}\int_{\mathrm{primary}} (\rho + p)e^{\Phi+\lambda}r^{2l}$$
$$\times \left[-e^{-\lambda}(\bar{V}_{nl}W_{nl} + \bar{W}_{nl}V_{nl}) + V_{nl}\bar{V}_{nl}\right]\mathrm{d}r. \tag{71}$$

In the Newtonian limit, this agrees with that of Unno et al. (1979) and Strohmayer (1991).

Fixing $\delta = 0.005$, we plot C_{nl} of g_1 modes (C_{12}, top panel) and of g_2 modes (C_{22}, bottom panel) as functions of compactness the mean density of the star in Fig. 10. The values for C_{12} and C_{22} differ only slightly (Yoshida & Lee 2000; Passamonti et al. 2009; Doneva et al. 2013), e.g. $C_{12} = 0.11$ and $C_{22} = 0.112$ for the star of WFF1 EOS that has $1.4\,\mathrm{M_\odot}$. On the other hand, we find that C_{n2} depends only slightly on stratification δ for $n \lesssim 5$, e.g. the difference between the values of C_{12} for $\delta = 0.001$ and 0.01 is ~ 0.001 (per cent level at most). The insignificant dependence on δ of C_{12} has also been shown in Gaertig & Kokkotas (2009).

6 CRUSTAL STRAIN

Having considered modulations in mode eigenfrequencies by tidal and magnetic fields, and the (slow) rotation of the equilibrium in Section 5, we now turn to investigate the maximal strain exerted on the stellar crust as a result of resonant g-mode displacements.

Time-varying displacements $\boldsymbol{\xi}$ between the material elements of the NS generates a stress. However, in GR, the total strain is not only due to the displacement, and there is a contribution from the perturbation of the metric to the strain tensor (Carter & Quintana 1972, 1975; Xu, Wu & Soffel 2001), whose total form reads

$$\sigma_{\mu\nu} = \frac{1}{2}\left(\nabla_\mu\xi_\nu + \nabla_\nu\xi_\mu\right) + \frac{1}{2}h^\eta_\mu h^\kappa_\nu\delta g_{\eta\kappa}$$
$$= \frac{1}{2}(\partial_\mu\xi_\nu + \partial_\nu\xi_\mu + \delta g_{\mu\nu}) - \Gamma^\sigma_{\mu\nu}\xi_\sigma, \tag{72}$$

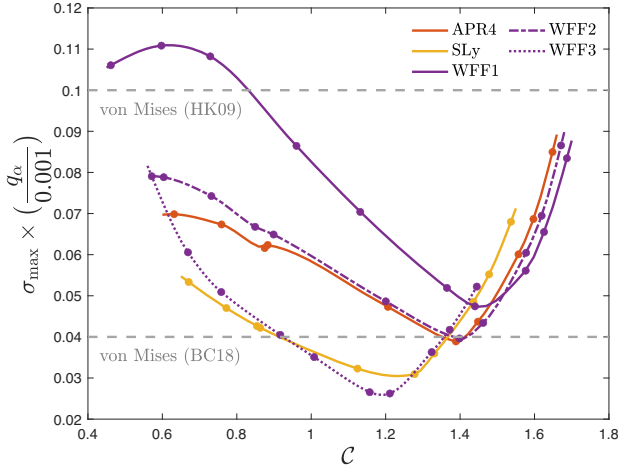**Figure 11.** Maximal crustal strain σ_{max} due to g_1 modes for APR4, SLy, and WFF1-3 EOS as functions of $\mathcal{C}$. The grey dashed line represents the von Mises criterion by Baiko & Chugunov (2018) and Horowitz & Kadau (2009). We have taken $\delta = 0.005$.

where we retain just the first order terms in the second line of the equation. Oscillations may lead to a crust failure for large enough stresses, which can be probed by the commonly used 'von Mises stress' criterion, coming from classical elasticity theory (Landau & Lifshitz 1959). Defining the strain as (Johnson-McDaniel & Owen 2013; Andersson et al. 2019)

$$\sigma \equiv \sqrt{\tfrac{1}{2}\sigma_{\mu\nu}\bar{\sigma}^{\mu\nu}}, \tag{73}$$

then the von Mises criterion implies that the crust breaks if σ exceeds some critical threshold, σ_{max}. In a recent semianalytic lattice stability models of Baiko & Chugunov (2018), they calculate the threshold as $\sigma_{max} \approx 0.04$ while Horowitz & Kadau (2009) follow molecular dynamics simulations to find $\sigma_{max} \approx 0.1$ for low-temperature stars. We adopt the former in this article with a remark that if the latter had been adopted, the amplitudes of resonantly-excited modes would need to be much higher to instigate failure.

Equation (72) and definition (73) indicate that the stress generated by the displacement ξ_α is proportional to its amplitude q_α, which evolves according to equation (19a). Therefore, we have

$$\sigma_\alpha(t) = \sqrt{2} \sum_\alpha \sqrt{q_\alpha(t)\bar{q}_\alpha(t)}\,\sigma_\alpha, \tag{74}$$

where σ_α is the *unit* strain caused by ξ_α (i.e. for $q_\alpha = 1$) and the pre-factor $\sqrt{2}$ is attributed to the duality of modes with ω and $-\bar{\omega}$.

Taking crust as the part of star with $0.9R_\star < r < R_\star$, in Fig. 11 we plot the maximal values of strain strain σ_{max} in the crust due to the ($l = m = 2$) g_1 modes for several EOS, where the stratification is taken to be $\delta = 0.005$. This latter value in particular is typical in the literature for mature NSs (Reisenegger 2009; Xu & Lai 2017). As such, relation (32) implies that g_1 modes with tidal coupling strength $\gtrsim 8 \times 10^{-5}$ may be capable of generating a crustal strain that exceeds the von Mises criterion provided $\omega M \sim 0.003$ for g_1 modes. We therefore conclude that tidal resonances in NSNS binaries can excite g modes to the point that the crust may yield, which can have important implications for observations of precursors of short gamma-ray bursts (Tsang et al. 2012; Suvorov & Kokkotas 2020). This latter aspect will be covered in detail in paper II.

In addition to low-order g modes, it has been shown by Passamonti et al. (2021) that the excitation of f modes before the merger, though not resonantly instigated, can generate a strain that meets the von

Mises criterion. For instance, we find the strain $\sigma_{max} = 0.107$ for the f mode of a particular primary with the SLy EOS and $M = 1.27\,\mathrm{M_\odot}$. However, only within less than 10 ms prior to the merger can σ_{max} hit the critical value of 0.04. Though the excited f modes are irrelevant to the precursors, their influences on the (phase of) GW waveforms may be measured with future GW detectors (see, e.g. Schmidt & Hinderer 2019; Pratten, Schmidt & Hinderer 2020).

7 DISCUSSION

The tidal field sourced by the companion as part of an NSNS binary perturbs the primary, leading to QNM excitations. In particular, as the perturbing frequency matches to the frequencies of certain QNMs, they will be brought into resonance, during which the mode amplitudes increase rapidly (Lai et al. 1994b; Kokkotas & Schafer 1995). Though mode resonances happen all during the inspiral, those that occur in the final stages are of particular interest in that modes with higher frequency couple more strongly to the tidal field, meaning larger amplitude become available during an appropriate resonance time-scale. If there is one resonantly excited mode that stresses the crust to the point beyond it cannot respond elastically, the crust may yield. For magnetized stars, the energy released by crustal failure is likely to generate electromagnetic flares (Tsang et al. 2012; Suvorov & Kokkotas 2020), which, in turn, offers a probe into the NS progenitor.

Our investigation on potential crust failure during the resonance between the tidal-driving frequency and the g modes of a strongly magnetized primary ($B_\star \sim 10^{15}$G), is divided into three parts: (i) Tidal excitation increases the mode amplitude to a maximum value that depends on the coupling strength of QNMs [see the fitting equation (32) for $l = 2$, g_1 modes, where the magnetic frequency shift and stellar rotation are ignored]. (ii) Mode frequencies are modified by magnetic fields, which become insignificant for purely poloidal fields with $B_\star \lesssim 10^{15}$G for $l = 2$, g_1 modes (Fig. 8; though if $\Lambda \ll 1$ weaker fields can still non-trivially modulate the spectrum); by tidal fields sourced the companion (equation 30), which are included only for completeness since they are negligibly small ($\lesssim 0.01$ per cent) for g modes; and by the (uniform) rotation (equation 70). (iii) The maximal strain during the resonance is estimated by the maximal amplitude of QNMs (equations 32 and 74).

Previous studies on tidally-driven crustal fracture use the Keplarian orbit, quadruple formula for GWs, tidal effects encoded in the Newtonian potential, and the stellar normal modes in the Newtonian theory (Tsang et al. 2012; Tsang 2013; Suvorov & Kokkotas 2020). In our calculation, several extensions are considered to better understand the realistic applicability of the mechanism, including 3 PN orbital evolution, relativistic pulsations, and several realistic EOS that pass the constraints set by GW170817 (Abbott et al. 2018). Our main results regarding the plausibility of g modes breaking the crust are summarized in Fig. 11.

Note that we have focused on g-mode resonances, though we include (slow) stellar rotation, which enriches the pulsation spectrum with r modes. The frequencies of these latter modes are comparable with those of g modes when the star rotates slowly, and thus may also be of interest in this scenario. In addition, our estimation on the maximal strain available in the g-mode resonances could be improved to better clarify the physical conditions under which crustal failure is possible. Namely, g-mode resonances are influenced by various parameters, including the mass of the primary $M_\star$ and the companion M_{comp} (or the mass ratio q between them), stratification δ of the primary, rotation frequency ν of the primary, characteristic magnetic strength $B_\star$, and the poloidal-to-toroidal strength Λ. An intensive

investigation of *g*-mode resonances over a multidimensional parameter space spanned by these parameters are, therefore, important to constrain the physical conditions that allow a large enough strain that may cause crust yielding. A forthcoming paper in this series aims to make progress in this direction.

DATA AVAILABILITY STATEMENT

Observational data used in this paper are quoted from the cited works. Data generated from computations are reported in the body of the paper. Additional data can be made available upon reasonable request.

REFERENCES

Abbott B. P. et al., 2017a, Phys. Rev. Lett., 119, 161101
Abbott B. P. et al., 2017b, ApJ, 848, L12
Abbott B. P. et al., 2017c, ApJ, 848, L13
Abbott B. P. et al., 2018, Phys. Rev. Lett., 121, 161101
Akgün T., Reisenegger A., Mastrano A., Marchant P., 2013, MNRAS, 433, 2445
Akmal A., Pandharipande V. R., Ravenhall D. G., 1998, Phys. Rev. C, 58, 1804
Alexander M. E., 1987, MNRAS, 227, 843
Andersson N., Ho W. C. G., 2018, Phys. Rev. D, 97, 023016
Andersson N., Kokkotas K. D., 1996, Phys. Rev. Lett., 77, 4134
Andersson N., Kokkotas K. D., 1998, MNRAS, 297, 493
Andersson N., Kokkotas K. D., 1998, MNRAS, 299, 1059
Andersson N., Kokkotas K. D., Schutz B. F., 1995, MNRAS, 274, 1039
Andersson N., Haskell B., Comer G. L., Samuelsson L., 2019, Class. Quantum Gravity, 36, 105004
Baiko D. A., Chugunov A. I., 2018, MNRAS, 480, 5511
Baiko D. A., Kozhberov A. A., 2017, MNRAS, 470, 517
Bauswein A., Janka H.-T., Oechslin R., 2010, Phys. Rev. D, 82, 084043
Bi S. L., Liao Y., Wang J. X., 2003, A&A, 397, 1069
Bildsten L., Cutler C., 1992, ApJ, 400, 175
Bini D., Damour T., Faye G., 2012, Phys. Rev. D, 85, 124034
Braithwaite J., 2009, MNRAS, 397, 763
Buonanno A., Damour T., 1999, Phys. Rev. D, 59, 084006
Carter B., Quintana H., 1972, Proc. R. Soc. A, 331, 57
Carter B., Quintana H., 1975, ApJ, 202, 511
Chan T. K., Sham Y.-H., Leung P. T., Lin L.-M., 2014, Phys. Rev. D, 90, 124023
Chandrasekhar S., 1956, ApJ, 124, 232
Chandrasekhar S., Fermi E., 1953, ApJ, 118, 116
Ciolfi R., Ferrari V., Gualtieri L., Pons J. A., 2009, MNRAS, 397, 913
Damour T., Jaranowski P., Schäfer G., 2000, Phys. Rev. D, 62, 044024
Detweiler S. L., Ipser J. R., 1973, ApJ, 185, 685
Detweiler S., Lindblom L., 1985, ApJ, 292, 12
Doneva D. D., Gaertig E., Kokkotas K. D., Krüger C., 2013, Phys. Rev. D, 88, 044052
Douchin F., Haensel P., 2001, A&A, 380, 151
Duncan R. C., Thompson C., 1992, ApJ, 392, L9
Ferrari V., Gualtieri L., Maselli A., 2012, Phys. Rev. D, 85, 044045
Finn L. S., 1986, MNRAS, 222, 393
Finn L. S., 1987, MNRAS, 227, 265
Friedman J. L., 1978, Commun. Math. Phys., 62, 247
Friedman J. L., Schutz B. F., 1975, ApJ, 200, 204
Fuller J., Kurtz D. W., Handler G., Rappaport S., 2020, MNRAS, 498, 5730
Gaertig E., Kokkotas K. D., 2009, Phys. Rev. D, 80, 064026
Glampedakis K., Lasky P. D., 2016, MNRAS, 463, 2542
Graber V., Andersson N., Glampedakis K., Lander S. K., 2015, MNRAS, 453, 671
Hartle J. B., 1967, ApJ, 150, 1005
Herbrik M., Kokkotas K. D., 2017, MNRAS, 466, 1330
Hinderer T. et al., 2016, Phys. Rev. Lett., 116, 181101
Ho W. C. G., Lai D., 1999, MNRAS, 308, 153
Horowitz C. J., Kadau K., 2009, Phys. Rev. Lett., 102, 191102
Hut P., 1981, A&A, 99, 126
Johnson-McDaniel N. K., Owen B. J., 2013, Phys. Rev. D, 88, 044004
Kantor E. M., Gusakov M. E., 2014, MNRAS, 442, L90
Kochanek C. S., 1992, ApJ, 398, 234
Kokkotas K. D., Schafer G., 1995, MNRAS, 275, 301
Kokkotas K. D., Apostolatos T. A., Andersson N., 2001, MNRAS, 320, 307
Krüger C. J., Kokkotas K. D., 2020, Phys. Rev. Lett., 125, 111106
Krüger C. J., Ho W. C. G., Andersson N., 2015, Phys. Rev. D, 92, 063009
Lai D., 1994, MNRAS, 270, 611
Lai D., 2001, Rev. Mod. Phys., 73, 629
Lai D., Rasio F. A., Shapiro S. L., 1993, ApJ, 406, L63
Lai D., Rasio F. A., Shapiro S. L., 1994, ApJ, 420, 811
Lai D., Rasio F. A., Shapiro S. L., 1994, ApJ, 423, 344
Landau L. D., Lifshitz E. M., 1970, Theory of Elasticity. Pergamon Press, New York
Lander S. K., 2013, Phys. Rev. Lett., 110, 071101
Lander S. K., Gourgouliatos K. N., 2019, MNRAS, 486, 4130
Landry P., Poisson E., 2015, Phys. Rev. D, 91, 104018
Lattimer J. M., Prakash M., 2001, ApJ, 550, 426
Lattimer J. M., Prakash M., 2007, Phys. Rev., 442, 109
Lau H. K., Leung P. T., Lin L. M., 2010, ApJ, 714, 1234
Lindblom L., Detweiler S. L., 1983, ApJS, 53, 73
Lockitch K. H., Andersson N., Friedman J. L., 2001, Phys. Rev. D, 63, 024019
McDermott P. N., 1990, MNRAS, 245, 508
McDermott P. N., van Horn H. M., Scholl J. F., 1983, ApJ, 268, 837
McDermott P. N., Hansen C. J., van Horn H. M., Buland R., 1985, ApJ, 297, L37
McDermott P. N., van Horn H. M., Hansen C. J., 1988, ApJ, 325, 725
Mastrano A., Melatos A., Reisenegger A., Akgün T., 2011, MNRAS, 417, 2288
Mastrano A., Suvorov A. G., Melatos A., 2015, MNRAS, 447, 3475
Nasiri S., Sobouti Y., 1989, A&A, 217, 127
Papadopoulos D., Esposito F. P., 1982, ApJ, 257, 10
Passamonti A., Haskell B., Andersson N., Jones D. I., Hawke I., 2009, MNRAS, 394, 730
Passamonti A., Andersson N., Pnigouras P., 2021, MNRAS, 504, 1273
Piro A. L., Bildsten L., 2005, ApJ, 619, 1054
Pnigouras P., 2019, Phys. Rev. D, 100, 063016
Poisson E., 2020, Phys. Rev. D, 101, 104028
Poisson E., Douçot J., 2017, Phys. Rev. D, 95, 044023
Pound A., 2012, Phys. Rev. Lett., 109, 051101
Pratten G., Schmidt P., Hinderer T., 2020, NatCo, 11, 2553
Press W. H., Teukolsky S. A., 1977, ApJ, 213, 183
Price R., Thorne K. S., 1969, ApJ, 155, 163
Radice D., Perego A., Zappa F., Bernuzzi S., 2018, ApJ, 852, L29
Read J. S., Lackey B. D., Owen B. J., Friedman J. L., 2009, Phys. Rev. D, 79, 124032
Reisenegger A., 2001, ApJ, 550, 860
Reisenegger A., 2009, A&A, 499, 557
Reisenegger A., Goldreich P., 1992, ApJ, 395, 240
Reisenegger A., Goldreich P., 1994, ApJ, 426, 688
Schaefer G., 1990, Astron. Nachr., 311, 213
Schmidt P., Hinderer T., 2019, Phys. Rev. D, 100, 021501
Schumaker B. L., Thorne K. S., 1983, MNRAS, 203, 457
Sotani H., 2016, Phys. Rev. D, 93, 044059
Sotani H., Kokkotas K. D., Stergioulas N., 2007, MNRAS, 375, 261

Steinhoff J., Hinderer T., Buonanno A., Taracchini A., 2016, Phys. Rev. D, 94, 104028

Strohmayer T. E., 1991, ApJ, 372, 573

Suvorov A. G., 2021, MNRAS, 503, 5495

Suvorov A. G., Kokkotas K. D., 2020, Phys. Rev. D, 101, 083002

Thorne K. S., Campolattaro A., 1967, ApJ, 149, 591

Troja E., Rosswog S., Gehrels N., 2010, ApJ, 723, 1711

Tsang D., 2013, ApJ, 777, 103

Tsang D., Read J. S., Hinderer T., Piro A. L., Bondarescu R., 2012, Phys. Rev. Lett., 108, 011102

Tsui L. K., Leung P. T., 2005, MNRAS, 357, 1029

Unno W., Osaki Y., Ando H., Shibahashi H., 1979, Nonradial Oscillation of Stars. University of Tokyo Press, Tokyo

Vavoulidis M., Kokkotas K. D., Stavridis A., 2008, MNRAS, 384, 1711

Vick M., Lai D., 2019, Phys. Rev. D, 100, 063001

Vines J. E., Flanagan É. É., 2013, Phys. Rev. D, 88, 024046

Völkel S. H., Krüger C. J., Kokkotas K. D., 2021, Phys. Rev. D, 103, 083008

Wasserman I., Shapiro S. L., 1983, ApJ, 265, 1036

Weinberg S., 1972, Gravitation and Cosmology: Principles and Applications of the General Theory of Relativity. Wiley-VCH, New York

Willems B., 2003, MNRAS, 346, 968

Wiringa R. B., Fiks V., Fabrocini A., 1988, Phys. Rev. C, 38, 1010

Wiringa R. B., Stoks V. G. J., Schiavilla R., 1995, Phys. Rev. C, 51, 38

Xu W., Lai D., 2017, Phys. Rev. D, 96, 083005

Xu C., Wu X., Soffel M., 2001, Phys. Rev. D, 63, 043002

Yoshida S., Eriguchi Y., 1999, ApJ, 515, 414

Yoshida S., Lee U., 2000, ApJS, 129, 353

Yu H., Weinberg N. N., 2017, MNRAS, 464, 2622

Zahn J.-P., 1977, A&A, 500, 121

Zahn J.-P., 2008, EAS Publ. Ser., 29, 67

Zhou Y., Zhang F., 2017, ApJ, 849, 114

This paper has been typeset from a TEX/LATEX file prepared by the author.